


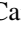





Wei, X., Li, X., Zhang, Z., Liermann, H.-P., Speziale, S., Pu, M., Zhang, C., Li, R., Yu, H., Li, L., Li, F., Zhou, Q. (2024): Impact of CaCl₂-induced chemical pressure on the phase transition of H₂O at high pressure. - Physical Review B, 109, 134108.

<https://doi.org/10.1103/PhysRevB.109.134108>

Impact of CaCl₂-induced chemical pressure on the phase transition of H₂O at high pressureXinmiao Wei ¹, Xinyang Li,^{1,2,3,*} Zihan Zhang,¹ Hanns-Peter Liermann ², Sergio Speziale,³ Mengqiong Pu ¹,
Caizi Zhang ¹, Ruiyu Li,¹ Hongyu Yu,¹ Liang Li ¹, Fangfei Li ^{1,†} and Qiang Zhou^{1,‡}¹*Synergetic Extreme Condition User Facility, State Key Laboratory of Superhard Materials, College of Physics, Jilin University, Jilin 130012, China*²*Deutsches Elektronen-Synchrotron DESY, Notkestraße 85, 22607 Hamburg, Germany*³*GFZ German Research Centre for Geosciences, Telegrafenberg, 14473 Potsdam, Germany* (Received 8 January 2024; revised 18 February 2024; accepted 28 March 2024; published 12 April 2024)

Understanding the phase behavior and structural properties of salt water at high pressures is essential for understanding the dynamics and physical characteristics of icy planets. In this study, we employed high-pressure experimental and *ab initio* simulation techniques to investigate the impact of CaCl₂ on the structure of ice VII. Our findings reveal that 1.8 mol% CaCl₂ can be incorporated into the ice VII structure above 10 GPa. This CaCl₂-bearing ice VII (Cb VII) exhibits a lower O-H stretching frequency in the Raman spectra as well as a reduced volume of the unit cell compared to pure ice VII. In contrast to doping ice VII with other salts such as LiCl and NaCl that leads to an increase of the ice VII to ice X transition pressure occurring at 100–150 GPa, CaCl₂ doping stands out by reducing the transition pressure. It shifts the transition to a pressure of 52 GPa, which is significantly lower than the transition pressure of 80 GPa in the pure H₂O ice system. This notable distinction highlights the unique influence of CaCl₂ on the phase behavior of water under high pressure, and we attribute these effects to the phenomenon of chemical pressure induced by CaCl₂ within the ice VII structure. Our study suggests that the presence of a modified ice VII phase, contaminated with salt and referred to as Cb VII, may influence the composition, structure, and evolution of planets.

DOI: [10.1103/PhysRevB.109.134108](https://doi.org/10.1103/PhysRevB.109.134108)**I. INTRODUCTION**

Water is abundantly found in numerous planets [1] and more than 20 unique stable and metastable polymorphs have been found using Raman spectroscopy, x-ray, and neutron diffraction techniques so far due to the diversity of the intermolecular hydrogen bond networks [2–7]. Ice VII, considered one of the most stable phases that forms when H₂O is pressurized above 2 GPa, is a solid with a body-centered cubic (bcc) arrangement of oxygen atoms [8]. The water molecules in ice VII are connected by hydrogen bonds (O-H···O). Pressure increases the length of covalent O-H bonds and reduces that of O···H bonds, enhancing the correlation of water molecules in the intermolecular hydrogen bond networks. Therefore, under high pressure, ice VII undergoes a proton order-disorder transition, transforming into a distinct stable phase known as ice X [9,10]. Ice X shares the same bcc oxygen lattice as ice VII but exhibits symmetrically placed hydrogen atoms between two oxygen atoms (O-H-O) [11]. Despite the general consensus on this fundamental change in O-H bond character under high pressures, significant discrepancies persist regarding the phase boundary between ice VII and ice X, with reported transition pressures varying from 40 GPa to above 120 GPa at room temperature [4,11–20].

The physical properties of polymorphs ice VII and ice X are pivotal factors that shape the structure and evolution of planetary bodies abundant in H₂O [11,21], e.g., in the icy environment of Ganymede, one of Jupiter's moons, and icy giant planet Uranus, which possess ice layers extending across the stability fields of both ice VI and ice X [22]. The recent discovery of salt solutions being ejected from icy planets has sparked the interest of researchers studying the interaction between salt and H₂O ices [21,23,24]. In the study conducted by Klotz *et al.* [25], it was reported that ice VII has the ability to incorporate approximately 15 mol% of LiCl during its transition from the glassy (amorphous) state to a crystalline form at 260–280 K and 4 GPa. Furthermore, Frank *et al.* [26] reported the incorporation of 2.4 mol% NaCl into ice VII at room temperature. Due to the replacement of water molecules in the crystal structure of ice VII with Li⁺, Na⁺, and Cl⁻ ions, and the disruption of perfect intermolecular hydrogen bond networks, the incorporation of LiCl and NaCl in H₂O ice significantly influence the behaviors of this ice at high pressure. The studies revealed that 2 mol% NaCl/LiCl presence suppresses proton order and hydrogen bond symmetrization and increases the pressure for the ice VII to ice X phase transition by ~30 GPa as shown by Raman spectroscopy studies and *ab initio* simulations [27,28]. The hinderance of proton order and hydrogen bond symmetrization caused by the incorporation of salt is the primary factor contributing to the increase in transition pressure, significantly affecting the magnetic field characteristics of Uranus and Neptune [25,26].

*Corresponding author: lixinyang@jlu.edu.cn†Corresponding author: lifangfei@jlu.edu.cn‡Corresponding author: zhouqiang@jlu.edu.cn

The different radii of salt ions lead to the formation of distinct intermolecular hydrogen bond networks when they replace water molecules. Thus, the doping effect of these monovalent chlorides on the ice VII lacked consistency [25,26,29]. Compared to lithium and sodium, potassium exhibits a larger radius, which makes it difficult to incorporate KCl into ice VII [25,29–31]. Except for alkali metals, six coordinating alkaline-earth-metal Mg^{2+} ions, which have a similar atomic radius to lithium, were discovered in the intermolecular hydrogen bond networks in MgCl_2 -bearing ice VII [31]. Calcium exhibits the largest radius after potassium among the major (i.e., most common) alkali metals and alkaline-earth metals, so it is expected to significantly influence the intermolecular hydrogen bond networks after incorporation.

In fact, ions with specific ionic radii and charges can induce chemical pressure in a crystal lattice, thereby influencing the crystal's properties. This phenomenon represents the concept of chemical pressure, wherein high-pressure phases can be produced at moderate pressures through the incorporation of ions, leading to a range of unique properties in the resulting material [32,33]. This concept has significant implications, particularly in the field of designing superconducting hydrides, where the pressure required for hydrogen metallization can be reduced through the use of different ion radii as chemical compressors [34]. For example, doping ice II with NH_4F reduces the transition pressure to ice V formation and the stability field of ice II [24]. In this particular case, NH_4^+ and F^- display different polarity compared to the water molecules, causing defects that influence the proton order of the intermolecular hydrogen bond network. In the case of calcium, which has a larger ionic radius compared to lithium, sodium, and magnesium, its interaction with ice can potentially give rise to unforeseen phenomena. Understanding the effects of calcium ions on ice is not only important for the study of fluid inclusions in geochemistry [35], but also crucial for unraveling the structure and behavior of icy planets.

In this study, the pressurization and resulting crystallization of 1.8 mol% CaCl_2 solutions were studied through Raman scattering and x-ray diffraction (XRD) up to 64 GPa. The reason for selecting this concentration is its alignment with the concentrations of other salt solutions investigated in prior research, enabling a direct comparison between the results of ice VII and salt interactions [26,36]. We found that β - CaCl_2 tetrahydrate (β - $\text{CaCl}_2 \cdot 4\text{H}_2\text{O}$) formed at 2.1 GPa with ice VII, and dissociation started at ~ 10 GPa upon increasing pressure. The changes in O-H stretching frequencies and the volume of ice VII, following the dissociation of β - $\text{CaCl}_2 \cdot 4\text{H}_2\text{O}$, indicate a significant chemical pressure effect of Ca^{2+} and Cl^- on the structure of ice VII. Using density functional theory (DFT) computations, we have determined the structures of CaCl_2 -bearing ice VII (Cb VII), in which Ca^{2+} and Cl^- ions replaced two to eight water molecules in the supercell of ice VII, exhibiting a 3% reduction in volume compared to pure ice VII. The observed volume anomaly in ice VII between 26 and 45 GPa, coupled with the emergence of the ice X - T_{2g} Raman mode at around 52 GPa, demonstrates that the presence of Ca^{2+} and Cl^- ions leads to a decrease in the transition pressure from ice VII to ice X, further confirming the chemical pressure effect of CaCl_2 on ice.

II. EXPERIMENTAL METHODS

A. Preparation of sample and high-pressure experiments

Aqueous 1.8 mol% CaCl_2 solutions were prepared by dissolving 1.8 mol% of CaCl_2 (Sinopharm Chemical Reagent Co., Ltd.; $\geq 99.8\%$) powder in deionized water. The 1.8 mol% CaCl_2 aqueous solutions were then directly injected into the sample chamber of the diamond-anvil cells (DACs) using syringes, and the DACs were quickly sealed to prevent evaporation loss of H_2O . For Raman spectroscopy, BX-90 type DACs with a 90° opening angle were used in the experiment. The diamond anvils were brilliantly cut and had culets with a diameter of 300 μm . T301 stainless-steel foil was indented to a thickness of 30 μm , and cylindrical sample chambers were produced by drilling 150 μm diameter holes using a laser drilling machine. For powder XRD experiments, normal symmetric DACs equipped with standard 300 μm diamond culets were used. The sample chamber was produced by laser drilling a preindented rhenium gasket with the same size as in the Raman-scattering experiment. A pressure medium was not used in our experiments because water is reactive with noble gas or other solid pressure mediums.

B. Raman scattering and powder XRD

High-pressure Raman spectra were collected using a LabRAM HR spectrometer (Horiba Jobin Yvon, France) equipped with a 600 gr/mm grating. A solid-state single longitudinal mode laser (MSL-FN-532, Changchun New Industries Optoelectronics Technology Co., Ltd, China) was used as the excitation source to irradiate the samples inside the DACs. To avoid potential heating of the samples, the laser power was kept at 2 mW, and the acquisition time was set to 60 s at each pressure point. The samples were compressed in steps of ~ 2 GPa up to ~ 64 GPa. The pressure was determined by measuring the pressure-induced shift of the R1 fluorescence line of a ruby sphere [37].

Powder XRD experiments were performed at the Extreme Conditions Beamline (P02.2) at PETRA III, Hamburg, Germany [38]. The energy of the beam was tuned to 25.68 keV (0.4828 \AA), while the beam was focused to $3 \times 8 \mu\text{m}^2$ ($H \times V$, full width at half maximum). Samples to detector distance and tilt of the detector were determined from powder XRD of the CeO_2 standard from NIST (674b) and analyzed with DIOP-TAS [39]. The DACs were pressurized using a gas-membrane system. A metallic doughnut-shaped He-filled membrane was placed in contact with the backside of the DAC. The stabilization time for each pressure point was about 5 min. Gold was used as the pressure calibrant, using the unit-cell parameters of gold powder (purity $> 99.95\%$) in conjunction with the pressure-volume equation of state (EoS) of Au [40].

C. DFT calculation

The DFT calculations were carried out using the software Vienna *ab initio* Simulation Package (VASP) using the projector-augmented wave method [41,42]. The cutoff energy was chosen to be 600 eV and the DFT-D3 method [43] was used for the vdW-dispersion energy-correction term in all the DFT calculations in this work. The valence electrons of the pseudopotentials are $1s^1$ for H, $2s^2 2p^4$ for O, $3s^2 3p^6 4s^2$

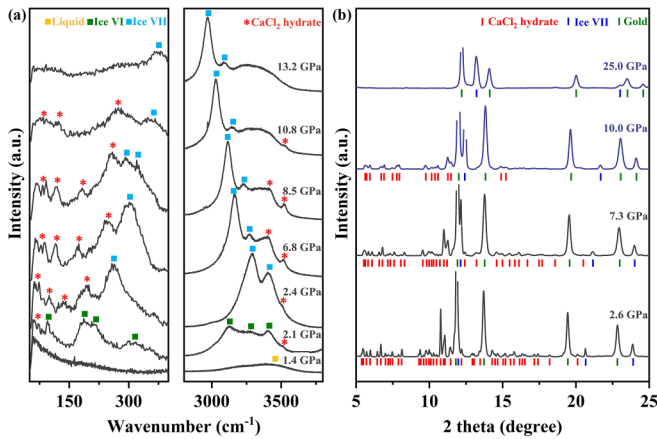


FIG. 1. (a) Representative Raman spectra of ice VI, ice VII, and CaCl_2 hydrate from the 1.8 mol% CaCl_2 solutions with increasing pressure at 298 K. The Raman modes of liquid, ice VI, ice VII, and CaCl_2 hydrate are indicated by yellow, green, and blue solid squares, and red solid stars, respectively. (b) XRD patterns of 1.8 mol% CaCl_2 solutions at high pressures and 298 K. The sequence of patterns represents the evolution during the compression experiment from 2.6 to 25 GPa. Colored tick marks show the diffraction peak positions of gold (green), ice VII (blue), and CaCl_2 hydrate (red). The patterns relative to undissociated CaCl_2 hydrate are plotted in black, while those of the dissociated CaCl_2 hydrate are plotted in blue.

for Ca, and $2s^2 2p^5$ for Cl. The exchange-correlation functional was described using Perdew-Burke-Ernzerhof (PBE) of generalized gradient approximation [44,45]. The combination of PBE with a vdW-D3 exchange-correlation functional was widely used in ice systems to consider the van der Waals (vdW) correction [46]. A Monkhorst-Pack k -point mesh of $2\pi \times 0.04$ and $2\pi \times 0.07 \text{ \AA}^{-1}$ were used for the structural relaxations of the supercell and *ab initio* molecular dynamics (AIMD), respectively. Ionic positions, cell volume, and cell shape were fully relaxed with a conjugate gradient algorithm. The AIMD simulations were carried out with a NVT ensemble at temperature 300 K using the initial structure from relaxation at 20 and 30 GPa, respectively. A Nose-Hoover thermostat was used for thermal bath of the NVT ensemble. We run 6 ps simulations with a time step of 0.5 fs. We used the positions of hydrogen from the crystal structure of ice VIII in our calculation of enthalpy because ice VIII [12], which exhibits the same positions of oxygen atoms as ice VII, is a more ordered phase with fixed positions of hydrogen at low temperatures. The supercells of CaCl_2 -bearing ice VII with different proportions and configurations were built as discussed in the Results and Discussions section.

III. RESULTS AND DISCUSSIONS

A. The formation and dissociation of $\beta\text{-CaCl}_2 \cdot 4\text{H}_2\text{O}$

Representative Raman spectra of ice polymorphs in experiments with 1.8 mol% CaCl_2 are shown in Fig. 1(a). Aqueous solutions of 1.8 mol% CaCl_2 were compressed from 1 bar to 17.7 GPa at 298 K. The liquid phase was only observed from 1 bar to 1.4 GPa [Fig. 1(a)]. When the pressure was increased to 2.1 GPa, an ice VI phase was formed, with Raman

peaks at around ~ 97 , 200, 3140, 3280, and 3410 cm^{-1} . In addition, two new peaks were observed at ~ 67 and 3510 cm^{-1} [Fig. 1(a)]. Ice VI transformed to ice VII [47] at 2.4 GPa and the two new peaks at ~ 67 and 3510 cm^{-1} were preserved across the transition, coexisting with ice VII. Besides the peaks of ice VII, four other new peaks at ~ 100 , ~ 140 , ~ 200 , and $\sim 3420 \text{ cm}^{-1}$ were observed, coexisting with ice VII up to 10.8 GPa [Fig. 1(a)]. To investigate the newly discovered Raman vibration peak, powder XRD experiments were conducted. Using a symmetric diamond-anvil cell, crystallization and phase transitions of the 1.8 mol% CaCl_2 solutions were investigated by powder XRD in the pressure range from 2.6 to 58 GPa. The XRD patterns display diffraction peaks characteristic of both gold (pressure marker) and ice VII at 2.6 GPa. Additional peaks were observed that cannot be attributed to any known crystalline phase in the H_2O system [Fig. 1(b)]. The newly observed diffraction lines remain stable in the pressure range from 2.6 to 10 GPa and disappear when the pressure reaches 25 GPa [Fig. 1(b)]. After comparing these new diffraction lines with those of the known CaCl_2 phases, we find that these new peaks cannot be indexed by any of the known CaCl_2 phases [48]. Using the refinement analysis of Le Bail, all new diffraction peaks could be indexed with the monoclinic unit-cell structure of $\beta\text{-CaCl}_2 \cdot 4\text{H}_2\text{O}$ reported earlier [49] (see Fig. S1 in the Supplemental Material [50] for the details of the refinement).

Compared with previous studies [51,52], our experimental results indicate that $\beta\text{-CaCl}_2 \cdot 4\text{H}_2\text{O}$ is more likely to form at high pressure than at ambient pressure. This may be attributed to the fact that $\beta\text{-CaCl}_2 \cdot 4\text{H}_2\text{O}$ has seven water molecules surrounding the Ca atom, which is different from the calcium chloride hydrates that are easily formed under ambient pressure, such as $\text{CaCl}_2 \cdot 2\text{H}_2\text{O}$, $\text{CaCl}_2 \cdot 4\text{H}_2\text{O}$ (α, γ), and $\text{CaCl}_2 \cdot 6\text{H}_2\text{O}$, which have four water molecules surrounding the Ca atom. Only under increasing pressure does the number of water molecules surrounding Ca increase. To further identify the Raman spectra of $\beta\text{-CaCl}_2 \cdot 4\text{H}_2\text{O}$ at high pressures, the stretching vibrational modes of pure ice VII (4.5 GPa) and ice VII with $\beta\text{-CaCl}_2 \cdot 4\text{H}_2\text{O}$ (4.4 GPa) were deconvoluted into three and four peaks using a Lorentz function, respectively [Fig. 2(a)]. The characteristic active Raman modes A_{1g} , E_g , and B_{1g} are observed in pure ice VII [53] [Fig. 2(a), lower panel]. Among the three modes, the A_{1g} mode ($\sim 3220 \text{ cm}^{-1}$) exhibits the highest intensity and corresponds to the in-phase symmetric O-H stretching [53]. The antisymmetric O-H stretching mode is attributed to the E_g mode ($\sim 3330 \text{ cm}^{-1}$), whereas the B_{1g} mode ($\sim 3400 \text{ cm}^{-1}$) is associated with the out-of-phase O-H stretching. The low intensity of the B_{1g} mode in comparison to the other two modes makes its identification difficult. When compared with pure ice VII, we found that $\beta\text{-CaCl}_2 \cdot 4\text{H}_2\text{O}$ has two new stretching modes at ~ 3400 and $\sim 3500 \text{ cm}^{-1}$, which is consistent with the findings in published literature [52]. The modes at $\sim 3400 \text{ cm}^{-1}$ of the $\beta\text{-CaCl}_2 \cdot 4\text{H}_2\text{O}$ overlap with the weak peak of B_{1g} of ice VII [Fig. 2(a), top panel].

However, when the pressure reaches 10 GPa, the identifiable XRD peaks associated with $\beta\text{-CaCl}_2 \cdot 4\text{H}_2\text{O}$ begin to decrease in intensity [Fig. 1(b)], accompanied by the disappearance of its Raman vibration modes at 10.8 GPa [Fig. 1(a)]. Upon reaching 25 GPa, a significant observation

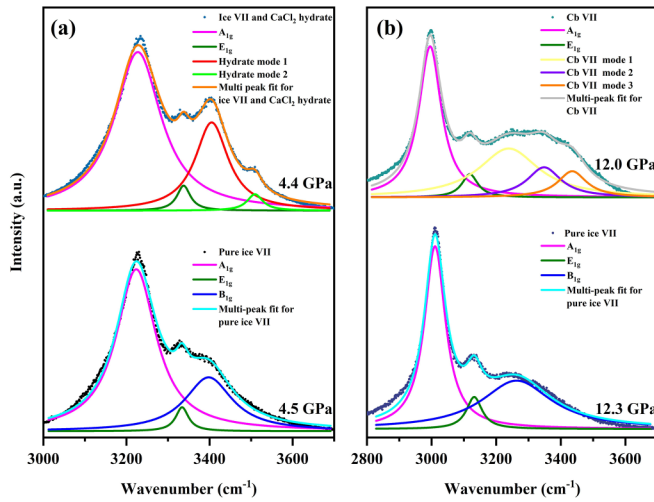


FIG. 2. (a) O-H stretching region of the Raman spectrum of pure ice VII and $\beta\text{-CaCl}_2 \cdot 4\text{H}_2\text{O}$. The cyan solid line shows the Lorentzian peak fit for signals of ice VII. A_{1g} , E_{1g} , and B_{1g} peaks of ice VII correspond to the pink, green, and blue solid lines, respectively. The orange solid line shows the double Lorentzian peak fit for signals of ice VII and $\beta\text{-CaCl}_2 \cdot 4\text{H}_2\text{O}$. The vibration modes 1 and 2 of $\beta\text{-CaCl}_2 \cdot 4\text{H}_2\text{O}$ are depicted in red and fluorescent green lines, respectively. The black and blue dotted lines represent our experimental results of pure ice VII and ice VII with $\beta\text{-CaCl}_2 \cdot 4\text{H}_2\text{O}$. (b) O-H stretching region of the Raman spectrum of pure ice VII and Cb VII. The green dotted lines represent our experimental result of Cb VII. The gray solid line shows the double Lorentzian peak fit for signals of ice VII and Cb VII. The vibration modes 1, 2, and 3 of Cb VII are depicted by yellow, purple, and yellow lines, respectively.

was the absence of any x-ray diffraction peaks corresponding to $\beta\text{-CaCl}_2 \cdot 4\text{H}_2\text{O}$, with only the x-ray diffraction peaks of ice VII and gold appearing in the pattern shown in Fig. 1(b). In addition, the high-energy high-pressure XRD diffraction spectra could not index the phase of CaCl_2 . Therefore, we conclude that the dissociation of $\beta\text{-CaCl}_2 \cdot 4\text{H}_2\text{O}$ starts at around 10 GPa and completes at 25 GPa, consistent with the results from other salt hydrates that dissociate when subjected to high pressure [54,55]. Unfortunately, the intensity of reflections was insufficient for structure refinement of the transitional dissociation of phase in $\beta\text{-CaCl}_2 \cdot 4\text{H}_2\text{O}$.

B. The formation of CaCl_2 -bearing ice VII

Upon the dissociation of $\beta\text{-CaCl}_2 \cdot 4\text{H}_2\text{O}$, a comparison of the Raman peaks in the O-H stretching region between the ice VII still present and the pure ice VII [at 12.3 GPa; Fig. 2(b), lower panel] unveiled the presence of new modes at 12 GPa. These new modes were deconvoluted into three peaks using Lorentzian peak shapes [Fig. 2(b), top panel]. In order to understand the origin of these newly discovered vibration modes, the O-H stretching frequency of ice VII, which had been formed from the 1.8 mol% CaCl_2 solutions, was thoroughly analyzed [Fig. 3(a)]. The O-H stretching frequency of this ice VII was found to vary inversely with pressure; that is, the O-H bond length increases with raising pressure and the O-O distance in the O-H-O unit decreases [56,57]. The O-H stretching frequency of ice VII crystallized from

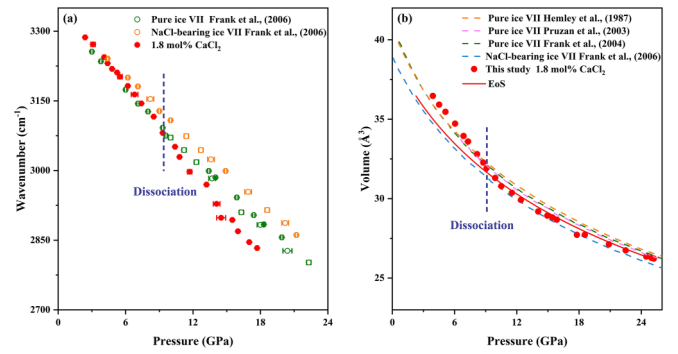


FIG. 3. (a) Evolution of $\Delta\nu_{\text{OH}}$ (cm^{-1}) as a function of pressure for ice VII formed from a 1.8 mol% CaCl_2 solution. Data from this study are depicted in red solid circles. The open circles represent the results of previous experiments [26]. The purple dashed line represents the pressure at which $\beta\text{-CaCl}_2 \cdot 4\text{H}_2\text{O}$ undergoes dissociation. (b) P-V relations of CaCl_2 -bearing ice VII, NaCl -bearing ice VII, and pure ice VII. Data from this study are depicted in red solid circles. The red solid line shows the fitting results using the third-order Birch-Murnaghan EoS in this study. The dashed lines represent the results of previous experiments [10,26,59,60].

1.8 mol% $\text{CaCl}_2\text{-H}_2\text{O}$ and that of pure H_2O [26,58] is in good agreement in the pressure range from 1 bar to 10 GPa [Fig. 3(a)]. At pressures of 10–26 GPa, as $\beta\text{-CaCl}_2 \cdot 4\text{H}_2\text{O}$ undergoes dissociation, the O-H stretching frequency of ice VII crystallized from 1.8 mol% $\text{CaCl}_2\text{-H}_2\text{O}$ exhibits a 10% lower frequency compared to pure ice VII [26,58] [Fig. 3(a)]. We speculate that during the dissociation of $\beta\text{-CaCl}_2 \cdot 4\text{H}_2\text{O}$, the Ca^{2+} or Cl^- ions might be incorporated into the structure of ice VII, similarly to other salt ions, thus influencing the O-H stretching frequency [26]. Although some CaCl_2 may not have fully dissolved into ice VII, its content is certainly below the resolution of our experimental detection. The experimental results, which demonstrate an elevated O-H stretching frequency for NaCl [26] and a reduced frequency for CaCl_2 [Fig. 3(a)], can be attributed to the abundance of Cl^- ions. This will be further explained in a following section.

The speculation of Ca^{2+} or Cl^- ions incorporation in ice VII is further supported by the pressure-volume (P-V) relations within the pressure range of 10–26 GPa, as depicted in Fig. 3(b). It is evident that the volume of ice VII after dissociation of $\beta\text{-CaCl}_2 \cdot 4\text{H}_2\text{O}$ deviates from that of pure ice VII, while following the trend of NaCl -bearing ice VII studied by Frank *et al.* [26]. The volume/pressure curve of ice VII between 2 and 10 GPa agrees with that of previous studies determined for pure ice VII [10,59,60] [Fig. 3(b)]. By utilizing the third-order Birch-Murnaghan EoS, we fit our data for ice VII formed from a CaCl_2 -bearing ice VII (Cb VII) within the 10–26 GPa pressure range and show a measurable depression in unit-cell volume compared to pure ice VII [Fig. 3(b)]. The values determined for the isothermal bulk modulus (K_{T0}), its pressure derivative ($K_{T'}$), and the volume at zero pressure (V_0) in ice VII (1.8 mol% CaCl_2) are 28.2 ± 0.3 GPa, 4.1 ± 0.1 , and $39.1 \pm 0.1 \text{ \AA}^3$, respectively. This behavior resembles the findings reported by Frank *et al.* [26] for NaCl -bearing ice VII, where they observed values of K_{T0} as 26.2 ± 1.4 GPa, $K_{T'}$ as 4.08 ± 0.18 , and V_0 as $39.1 \pm 0.2 \text{ \AA}^3$ [26]. Hence, in the context of the dissociation process of $\beta\text{-CaCl}_2 \cdot 4\text{H}_2\text{O}$, it

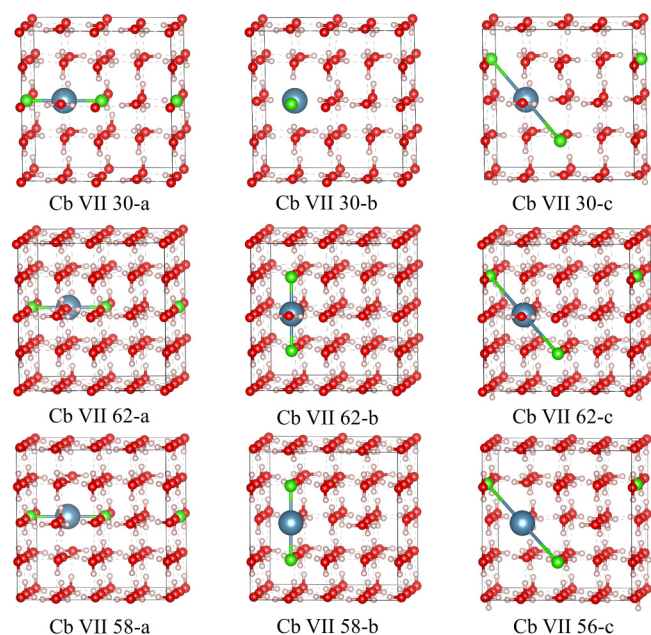


FIG. 4. Illustrations of nine different CaCl₂ configurations in ice VII structure before ionic relaxation. Different color spheres in the sites represent H (pink), Ca (blue), Cl (green), and O (red) atoms, respectively.

is suggested that the Ca²⁺ and Cl⁻ ions are incorporated in the ice VII structure, leading to the formation of CaCl₂-bearing ice VII (Cb VII).

C. The chemical pressure effect of CaCl₂ on ice

The incorporation of Ca²⁺ and Cl⁻ ions resulted in a reduction in the volume of the ice phase by approximately 3% compared with pure ice VII at pressures ranging from 10 to 26 GPa [Fig. 3(b)]. However, the volume of ice VII increased after incorporating LiCl and MgCl₂ as described in other studies [25,31]. The volume reduction we observe in the system H₂O-CaCl₂ can be interpreted as the effect of the chemical pressure of ice due to the incorporation of CaCl₂, and is similar to the behavior of the system H₂O-NaCl. This phenomenon is potentially induced by the larger radii of Ca²⁺ and Na⁺ compared to Li⁺ and Mg²⁺, where the magnitude of the chemical pressure depends on the radii of the cations incorporated in intermolecular hydrogen bond networks. The substitution of larger cations for a large quantity of water molecules within the intermolecular hydrogen bond network leads to the compression of the surrounding ice lattice.

To microscopically clarify chemical pressure through CaCl₂ incorporation in the crystal structure of ice, we carried out *ab initio* simulations of supercells with 32 and 64 water molecules of ice VII, where two to eight water molecules were replaced with one Ca²⁺ and two Cl⁻ ions as shown in Fig. 4 (all structures presented in the figure were drawn using VESTA [61]). These configurations were widely used in the salt-bearing ice VII simulations [25,28,31]. In the nine configurations, Ca²⁺ ions are located at sites with the six-fold coordination (the surface center of bcc lattice). This is because cations exhibit larger volume and higher coordination compared to water molecules, allowing them to typically

occupy the surface of the oxygen bcc sublattice in salt-bearing ice [25,28,31]. On the other hand, anions have a similar volume to water molecules but possess a negative charge. As a result, anions typically replace water molecules in the hydrogen bonding network. To consider the local charge of replacements and computational cost, we constructed three different configurations with different neighbor relationships between Ca²⁺ and Cl⁻ ions. Two nearest neighbor, next nearest neighbor, and third neighbor water molecules were replaced with two Cl⁻ ions in configurations a, b and c, respectively, as observed in the ice VII structure bearing MgCl₂ [31].

As shown in Fig. 4, structures of Cb VII 30-a (b or c) and Cb VII 62-a (b or c) were built in configurations a (b or c) with 2×2×1 and 2×2×2 supercells, respectively. Due to the larger radius of the Ca²⁺ ion compared to the Mg²⁺ ion, we induced defects of four water molecules and six water molecules around the Ca²⁺ ion in the 2×2×2 supercells, as illustrated in Cb VII 58-a (b) and Cb VII 56-c, respectively. All nine configurations were predicted to exhibit slightly positive formation enthalpies, decomposing into ice VII and CaCl₂ (Fig. S2 [50]). It is notable that positive formation enthalpy in crystal defects is quite common. For instance, the formation enthalpy of point defects in GaN is approximately 80 meV/atom [62], which is of the same order of magnitude as our research findings on Cb VII. Structures Cb VII 58-a, 58-b, and 56-c, which were built with more defect water molecules in the supercell, exhibited lower enthalpy than structures Cb VII 30-a, 30-b, 30-c, 62-a, 62-b, and 62-c (Fig. 4). As the initial structures could clarify the relative position of Ca²⁺ and Cl⁻ ions, we chose them to introduce our configurations. The structures after optimization are shown in the Supplemental Material (Fig. S3 [50]). As a result of the large radius of Ca²⁺ ions, incorporation of CaCl₂ into ice VII will cause more defects in the intermolecular hydrogen bond networks than in the case of MgCl₂-bearing ice [31]. Therefore, the properties of Cb VII may be significantly different from pure ice VII due to chemical pressure induced by the Ca²⁺ ions. Figure 5 illustrates the reduction of volumes resulting from the inclusion of CaCl₂ within each of the modeled ice VII crystal configuration, as determined through DFT calculations within the pressure range of 5–20 GPa. The volume decrease exceeded 2.5% when the pressure exceeded 15 GPa in Cb VII 56-c, aligning closely with our experimental results (3%; Fig. 5). Thus, we postulate that the new ice VII that formed with the changed volume is Cb VII 56-c. In fact, the 56-c configuration exhibits similar concentration to that in experiment (1.8 mol%, 1:56 = 0.0179).

According to our XRD and DFT results, the volume of ice VII [Fig. 3(b); 5] decreases as a result of larger amounts of Ca²⁺ ions being incorporated into its structure. Intuitively, one would expect the volume of the structure to increase due to the larger ionic radii of Ca²⁺. However, the effect on the intermolecular hydrogen bond networks counteracts this expectation. This phenomenon we observe in Cb VII is commonly known as chemical-pressure-induced volume reduction. This represents the first aspect of chemical pressure induced by calcium chloride.

The findings of an earlier study indicate that the ion-induced electric polarity has a greater quantity effect on the volume of the ice structure over long distances, as opposed to

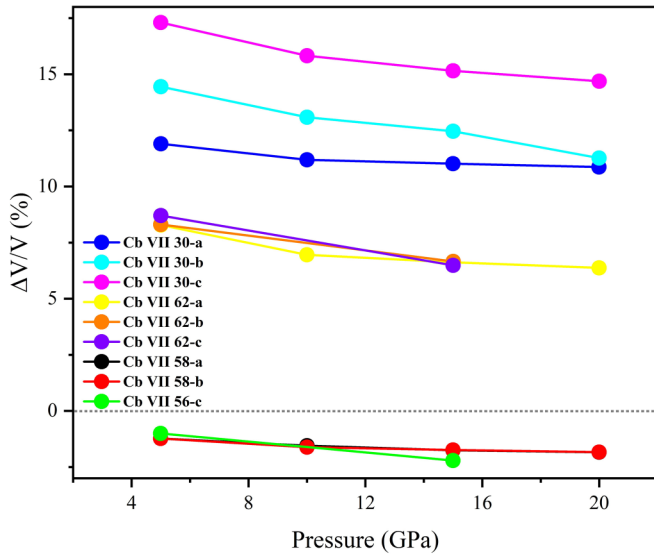


FIG. 5. The percentage change in volume from *ab initio* calculations between each water molecule in the nine configurations and each water molecule in ice VII under different pressures. The gray dashed line represents the volume of ice VII from DFT calculations. Different color solid circles represent the percentage increase in calculated volume of Cb VII 30-a (blue), 30-b (cyan), 30-c (pink), 62-a (yellow), 62-b (orange), 62-c (purple), 58-a (black), 58-b (red), and 56-c (green), respectively. The data of Cb VII 58-b overlaps with the data of Cb VII 58-a.

the local geometric distortions arising from ion incorporation, which would increase the volume [63]. Therefore, the electric field generated by Cl^- and Ca^{2+} ions is the major factor responsible for the decrease in volume of ice VII. Furthermore, the changes in electric field caused by these ions affect the nuclear quantum effects (NQE) within the ice, ultimately influencing the transition pressure from ice VII to ice X [63]. As previously described, the O-H covalent bond undergoes elongation, and the distance of the H \cdots O hydrogen bond experiences shortening as pressure increases. This triggers the conversion of ice VII to ice X, positioning the hydrogen atom at the midpoint between the O atoms [11,64]. In pure ice, NQEs play a crucial role by significantly lowering the phase transition pressure points of ice VII-X. As the O-O distance decreases with increasing pressure, the carrier population between the two potential wells of the O-H \cdots O coordinate diminishes, while the proton tunneling frequency increases (indicating the presence of NQEs that become enhanced with increasing pressure). The presence of salt ions generates an induced electric field, which limits the orientational freedom of water molecules and influences NQEs, depending on their proximity to the anions or cations of the salt [63]. This is consistent with the findings in Bronstein *et al.* [27], where LiCl/NaCl leads to an increase in the phase transition pressure between ice VII and ice X. Essentially, this is attributed to the induced electric field generated by the ions, which in turn affects NQEs. However, the simulations in VASP did not account for NQEs and further calculations involving NQEs should be conducted in the future.

Bronstein *et al.* [27] established that the transition pressure from ice VII to ice X is independent of the type or size of

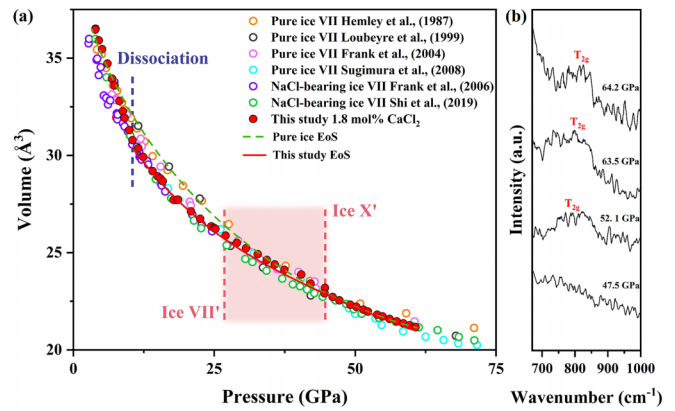


FIG. 6. (a) Unit-cell volume of pure and salty ice at high pressures and 298 K. Red solid circles represent our experimental result. Green dashed circles: NaCl-bearing ice VII (Frank *et al.* [36]); purple dashed circles: NaCl-bearing ice VII (Shi *et al.* [65]); orange circles: pure ice (Hemley *et al.* [10]); pink circles: pure ice (Frank *et al.* [59]); cyan circles: pure ice (Sugimura *et al.* [16]). The pink shade indicates the pressure range for the dynamically disordered ice X' estimated from XRD measurements. (b) Evolution of the ice X- T_{2g} mode on compression above 47 GPa. The solid red line represents the EoS of this study. The green dashed line represents the EoS of pure ice VII.

the cationic impurity (Li^+ and Na^+ ions) incorporated within the ice VII structure. However, it also has been reported that defects caused by impurities with different polarity could influence proton order, leading to a change of the phase diagram of ice [24]. In particular, it has been speculated that the emergence of the ice X signal, as evident in the change of the slope of O-H stretching band frequency as a function of pressure, could be caused by the defects of anions (Cl^- ions), which display different polarity compared to the water molecule. In Cb VII, the larger quantity of Cl^- ions present is anticipated to result in a different O-H stretching behavior compared to that in NaCl-bearing and LiCl-bearing ice VII. Previous studies by Frank *et al.* [26] further support this finding, with Fig. 3(a) illustrating a different (qualitatively opposite) effect of 1.8 mol% NaCl and 1.8 mol% CaCl_2 on the O-H stretching in ice VII compared to pure ice VII. As a result, the presence of Cl^- within the bcc site of ice VII is anticipated to trigger rotation in the surrounding water molecules, orienting the hydrogens towards the Cl^- ion to influence the proton order of ice, and thus change the phase diagram. Specifically, in Cb VII, Cl^- ions impact its quantum effects, altering the transition pressure from ice VII to ice X, and exhibiting chemical pressure of the water molecule network. This represents the second aspect of chemical pressure induced by CaCl_2 .

Research indicates that the transition from ice VII to ice X in pure ice occurs in stages, involving compressible dynamically disordered ice VII (ice VII'), disordered ice X (ice X'), and ultimately ice X [11,16]. This transition from ice VII' to ice X' can be well determined by the decrease in bulk modulus for both pure and salt-bearing ice [11,58,65]. Figure 6(a) presents the volume of ice VII from our experiment performed in the pressure range from 10 to 60 GPa (the formation of Cb VII), while also displaying a comparative analysis of previous measurements on pure ice VII [4,10,16,59] and NaCl-bearing

ice VII (1.9 mol% NaCl) [65,66]. We observed that the volume of Cb VII has a 3% decrease compared to pure ice VII except for an anomaly detected at 26 and 45 GPa [Fig. 6(a)]. This anomaly shows a 3% volume increase compared to Cb VII at 10–26 GPa and 45–60 GPa. The volume increase within this pressure range contributes to the decrease in bulk modulus, consistent with the decrease caused by the transition from ice VII' to ice X'. Therefore, we attribute this change to the transition from a dynamically disordered state of ice VII' to ice X' [11,58,65]. In pure ice VII, Sugimura *et al.* [16] reported that the pressure at which the transition from ice VII to dynamically disordered ice VII' occurs is about 40 GPa. Méndez *et al.* [11] argue that the transition of ice VII to ice VII' and ice X' occurs at 35–55 GPa by conducting quasi-continuous synchrotron time-resolved XRD experiments. In comparison, our results indicate that the inclusion of Ca²⁺ and Cl⁻ ions results in a decrease of approximately 5–10 GPa for the transition pressure from ice VII' to ice X' for Cb VII [11,16,19,67]. Therefore, the findings from our XRD experiment validate the hypothesis of the chemical pressure effect exerted by 1.8 mol% CaCl₂ on ice.

Our Raman-scattering experiments provide further confirmation of this finding, indicating that the presence of Ca²⁺ and Cl⁻ ions promotes the transition of ice VII to ice X at lower pressures. Figure 6(b) demonstrates the detection of a single O-O vibrational mode with T_{2g} symmetry at 52 GPa, which is widely used to identify the transition from ice VII to the cuprite-type structure of ice X [18,68]. The transition pressure for the detection of T_{2g} in this study was found to be 30 GPa lower than the findings of Goncharov *et al.* [68] who reported the presence of T_{2g} in pure ice X at 80 GPa. This transition pressure is lower than that of LiCl and NaCl-bearing ice VII. The transition pressure from phase ice VII to phase ice X increases to 100–150 GPa with the incorporation of 1.9–7.7 mol% Li/NaCl into ice VII [27,28]. As we previously speculated, this difference may be contributed to the chemical pressure caused by 1.8 mol% CaCl₂. The surface of Europa may have 4 mol% Ca, according to earlier studies, as it has at least 10 mol% Na₂SO₄, Na/K, and Ca/K ratios of 30 and 6, respectively. Consequently, it can be said that CaCl₂ from the icy planets may be able to cause chemical pressure on ice VII [69,70].

To further understand this observation, we examined the radial distribution function (RDF) of OH in pure ice VII and that of Cb VII at 30 GPa, which was calculated from *ab initio* molecular dynamics as shown in Fig. 7. At 30 GPa, in ice VII, the RDF of the OH bond shows two peaks that denote two different bond lengths (Fig. 7), corresponding to short covalent O-H bonds (around 1 Å) and long hydrogen O···H bonds (around 1.6 Å). With increasing pressure, the covalent O-H bonds become longer and the hydrogen O···H bonds become shorter. Finally, the two peaks of the RDF broaden significantly and merge into the single one when ice X forms. At the same pressure, the covalent O-H bonds are essentially as long in pure ice as in Cb VII, but the distribution (peak width) is larger with a tail towards longer values in Cb VII 56-c. The hydrogen O···H bonds are longer in pure ice VII (Fig. 7). The same trend is observed in calculations conducted at 20 GPa (Fig. S4 [50]). These results indicated that symmetrization of hydrogen bonds could emerge in Cb

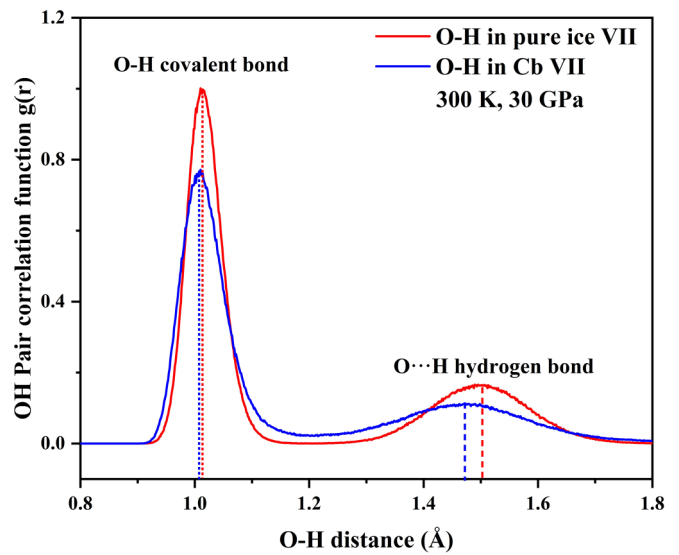


FIG. 7. Radial distribution function $g(r)$ of the distance OH below the transition (in phase VII at approximately 30 GPa) in pure ice VII (in red) [63] and in CaCl₂-bearing ice VII (in blue), obtained from quantum thermal bath molecular dynamics. The dotted lines indicate the average OH covalent bond length, while the dashed lines indicate the average O···H hydrogen bond length.

VII at lower pressure than that in pure ice VII. There is a difference between the phenomenon of lowering the pressure point of hydrogen bond symmetrization in Cb VII and LiCl/NaCl-bearing ice VII. The widths of the peaks in the OH RDF for covalent O-H bonds and hydrogen O···H bonds in LiCl/NaCl-bearing ice VII are comparatively narrower than those in pure ice, which hinders the phase transition from ice VII to ice X [29,30]. This contradicts Cb VII calculations that indicated wider peaks in the RDF compared to pure ice (Fig. 7). This observation may explain why Cb VII observed a volume anomaly at 26–45 GPa compared to pure ice VII, while NaCl-bearing ice VII observed a volume anomaly at 40–60 GPa [65] [Fig. 6(a)].

Therefore, the presence of CaCl₂ in ice VII may play a pivotal role in facilitating the transition from ice VII to ice X, due to the chemical pressure it exerts on the ice. Ice X may serve as an indicator of the imminent superionic phase emerging at higher pressures, yielding profound implications for our comprehension of dense matter and the inner workings of planetary structures. We think that the ionic impurity causing chemical pressure affects the high-pressure ice phase diagram strongly and thus demands further systematic investigation.

IV. CONCLUSIONS

This study investigates the effects of CaCl₂ on the structure of ice VII using high-pressure experimental and *ab initio* simulation techniques. Our results demonstrate that the structure of ice VII can incorporate 1.8 mol% CaCl₂ at pressures above 10 GPa, resulting in the formation of CaCl₂-bearing ice VII (Cb VII) with properties significantly different from those of pure ice VII. Specifically, Cb VII displays a lower O-H stretching frequency and a reduced volume of the crystal unit cell. Based on our DFT computations, different configurations

of Cb VII were modeled. The volume of Cb VII displays an anomaly within the pressure range of 26–45 GPa and Raman scattering reveals the presence of ice X– T_{2g} at 52 GPa, suggesting the chemical pressure effects originating from CaCl_2 affect the transition from ice VII to ice X. This is in contrast to NaCl/LiCl -bearing ice VII, which drives the transition from ice VII to ice X to higher pressures (100–150 GPa). This remarkable phenomenon highlights the unique influence of CaCl_2 on the phase diagram of water ice under high pressure. In this paper, we unveil the chemical pressure effect of bivalent chloride on the phase transition between ice VII and ice X, and it can potentially help to understand the composition, structure, and evolution of planets.

The dataset from this experimental work can be accessed at [71].

ACKNOWLEDGMENTS

We sincerely appreciate the valuable comments and suggestions provided by the two anonymous reviewers for this

paper. X.L. acknowledges support from the National Key Research and Development Project of China (Grant No. 2023YFF0804100). X.L., Q.Z., and F.L. acknowledge support from the National Natural Science Foundation of China (NSFC; 42102030, 12074141, and 12274168). X.L., H.-P.L. and S.S. acknowledge the scientific exchange and support of the Center for Molecular Water Science (CMWS) as part of the early science program (DESY and GFZ). This work was also supported by Jilin Provincial Science and Technology Development Project (Grants No. 20210402054GH and No. 20220101011JC) and the Program for Jilin University Science and Technology Innovative Research Team (Grant No. 2021-TD-05). We also acknowledge DESY (Hamburg, Germany), a member of the Helmholtz Association HGF, for the provision of the experimental facilities. The x-ray diffraction was carried out at beamline P02.2 and used facilities provided by the Extreme Condition Science Infrastructure (ECSI) of PETRA III. This work was partially carried out at the high-pressure synergetic measurement station of Synergic Extreme Condition User Facility.

-
- [1] S. A. Kattenhorn and L. M. Prockter, Evidence for subduction in the ice shell of Europa, *Nat. Geosci.* **7**, 762 (2014).
- [2] C. G. Salzmann, Advances in the experimental exploration of water's phase diagram, *J. Chem. Phys.* **150**, 060901 (2019).
- [3] I. M. Chou, J. G. Blank, A. F. Goncharov, H.-K. Mao, and R. J. Hemley, In situ observations of a high-pressure phase of H_2O ice, *Science* **281**, 809 (1998).
- [4] P. Loubeyre, R. LeToullec, E. Wolanin, M. Hanfland, and D. Häusermann, Modulated phases and proton centring in ice observed by X-ray diffraction up to 170 GPa, *Nature (London)* **397**, 503 (1999).
- [5] J.-F. Lin, B. Militzer, V. V. Struzhkin, E. Gregoryanz, R. J. Hemley, and H.-K. Mao, High pressure-temperature Raman measurements of H_2O melting to 22 GPa and 900 K, *J. Chem. Phys.* **121**, 8423 (2004).
- [6] S. Klotz, K. Komatsu, H. Kagi, K. Kunc, A. Sano-Furukawa, S. Machida, and T. Hattori, Bulk moduli and equations of state of ice VII and ice VIII, *Phys. Rev. B* **95**, 174111 (2017).
- [7] H. Fukui, H. Kadobayashi, H. Abe, R. Takahashi, H. Wadati, and N. Hirao, Equation of states for dense ice up to 80 GPa at low-temperature conditions, *J. Chem. Phys.* **156**, 064504 (2022).
- [8] R. J. Nelmes, J. S. Loveday, W. G. Marshall, G. Hamel, J. M. Besson, and S. Klotz, Multisite disordered structure of ice VII to 20 GPa, *Phys. Rev. Lett.* **81**, 2719 (1998).
- [9] W. F. Kuhs, J. L. Finney, C. Vettier, and D. V. Bliss, Structure and hydrogen ordering in ices VI, VII, and VIII by neutron powder diffraction, *J. Chem. Phys.* **81**, 3612 (1984).
- [10] R. J. Hemley, A. P. Jephcoat, H. K. Mao, C. S. Zha, L. W. Finger, and D. E. Cox, Static compression of H_2O -ice to 128 GPa (1.28 Mbar), *Nature (London)* **330**, 737 (1987).
- [11] A. S. J. Méndez, F. Trybel, R. J. Husband, G. Steinle-Neumann, H. P. Liermann, and H. Marquardt, Bulk modulus of H_2O across the ice VII–ice X transition measured by time-resolved x-ray diffraction in dynamic diamond anvil cell experiments, *Phys. Rev. B* **103**, 064104 (2021).
- [12] K. Aoki, H. Yamawaki, M. Sakashita, and H. Fujihisa, Infrared absorption study of the hydrogen-bond symmetrization in ice to 110 GPa, *Phys. Rev. B* **54**, 15673 (1996).
- [13] A. F. Goncharov, V. V. Struzhkin, M. S. Somayazulu, R. J. Hemley, and H. K. Mao, Compression of ice to 210 gigapascals: Infrared evidence for a symmetric hydrogen-bonded phase, *Science* **273**, 218 (1996).
- [14] E. Wolanin, P. Pruzan, J. C. Chervin, B. Canny, M. Gauthier, D. Häusermann, and M. Hanfland, Equation of state of ice VII up to 106 GPa, *Phys. Rev. B* **56**, 5781 (1997).
- [15] M. Somayazulu, J. Shu, C.-S. Zha, A. F. Goncharov, O. Tschauer, H.-K. Mao, and R. J. Hemley, *In situ* high-pressure x-ray diffraction study of H_2O ice VII, *J. Chem. Phys.* **128**, 064510 (2008).
- [16] E. Sugimura, T. Iitaka, K. Hirose, K. Kawamura, N. Sata, and Y. Ohishi, Compression of H_2O ice to 126 GPa and implications for hydrogen-bond symmetrization: Synchrotron x-ray diffraction measurements and density-functional calculations, *Phys. Rev. B* **77**, 214103 (2008).
- [17] M. Guthrie, R. Boehler, C. A. Tulk, J. J. Molaison, A. M. dos Santos, K. Li, and R. J. Hemley, Neutron diffraction observations of interstitial protons in dense ice, *Proc. Natl. Acad. Sci. USA* **110**, 10552 (2013).
- [18] C.-S. Zha, J. S. Tse, and W. A. Bassett, New Raman measurements for H_2O ice VII in the range of 300 cm^{-1} to 4000 cm^{-1} at pressures up to 120 GPa, *J. Chem. Phys.* **145**, 124315 (2016).
- [19] M. Guthrie, R. Boehler, J. J. Molaison, B. Haberl, A. M. dos Santos, and C. Tulk, Structure and disorder in ice VII on the approach to hydrogen-bond symmetrization, *Phys. Rev. B* **99**, 184112 (2019).
- [20] T. Meier, S. Petitgirard, S. Khandarkhaeva, and L. Dubrovinsky, Observation of nuclear quantum effects and hydrogen bond symmetrisation in high pressure ice, *Nat. Commun.* **9**, 2766 (2018).
- [21] B. Journaux, K. Kalousová, C. Sotin, G. Tobie, S. Vance, J. Saur, O. Bollengier, L. Noack, T. Rückriemen-Bez, T. Van

- Hoolst, K. M. Soderlund, and J. M. Brown, Large ocean worlds with high-pressure ices, *Space Sci. Rev.* **216**, 7 (2020).
- [22] C. Sotin, O. Grasset, and A. J. I. Mocquet, Mass–radius curve for extrasolar Earth-like planets and ocean planets, *Icarus* **191**, 337 (2007).
- [23] R. Cerubini, A. Pommerol, Z. Yoldi, and N. Thomas, Near-infrared reflectance spectroscopy of sublimating salty ice analogues. Implications for icy moons, *Planet. Space Sci.* **211**, 105391 (2022).
- [24] J. J. Shephard, B. Slater, P. Harvey, M. Hart, C. L. Bull, S. T. Bramwell, and C. G. Salzmann, Doping-induced disappearance of ice II from water’s phase diagram, *Nat. Phys.* **14**, 569 (2018).
- [25] S. Klotz, L. E. Bove, T. Strässle, T. C. Hansen, and A. M. Saitta, The preparation and structure of salty ice VII under pressure, *Nat. Mater.* **8**, 405 (2009).
- [26] M. R. Frank, C. E. Runge, H. P. Scott, S. J. Maglio, J. Olson, V. B. Prakapenka, and G. Shen, Experimental study of the NaCl – H₂O system up to 28 GPa: Implications for ice-rich planetary bodies, *Phys. Earth Planet. Inter.* **155**, 152 (2006).
- [27] Y. Bronstein, P. Depondt, L. E. Bove, R. Gaal, A. M. Saitta, and F. Finocchi, Quantum versus classical protons in pure and salty ice under pressure, *Phys. Rev. B* **93**, 024104 (2016).
- [28] Z. Raza Bove, A.-A. Ludl, S. Klotz, A. M. Saitta, A. F. Goncharov, and P. Gillet, Effect of salt on the H-bond symmetrization in ice, *Proc. Natl. Acad. Sci. USA* **112**, 8216 (2015).
- [29] A. A. Ludl, L. E. Bove, D. Corradini, A. M. Saitta, M. Salanne, C. L. Bull, and S. Klotz, Probing ice VII crystallization from amorphous NaCl–D₂O solutions at gigapascal pressures, *Phys. Chem. Chem. Phys.* **19**, 1875 (2017).
- [30] X. Wei, Q. Zhou, F. Li, C. Zhang, F. Sun, Z. Zhang, R. Li, H. Yu, Y. Yan, L. Li, H.-P. Liermann, S. Speziale, and X. Li, Novel high-pressure potassium chloride monohydrate and its implications for water-rich planetary bodies, *J. Geophys. Res.: Planets* **128**, e2022JE007622 (2023).
- [31] M. Watanabe, K. Komatsu, F. Noritake, and H. Kagi, Structural incorporation of MgCl₂ into ice VII at room temperature, *Jpn. J. Appl. Phys.* **56**, 05FB03 (2017).
- [32] N. W. Ashcroft, Hydrogen dominant metallic alloys: High temperature superconductors?, *Phys. Rev. Lett.* **92**, 187002 (2004).
- [33] H.-k. Mao, Harnessing chemical pressure, *Natl. Sci. Rev.* **10**, nwad234 (2023).
- [34] Z. Zhang, T. Cui, M. J. Hutcheon, A. M. Shipley, H. Song, M. Du, V. Z. Kresin, D. Duan, C. J. Pickard, and Y. Yao, Design principles for high-temperature superconductors with a hydrogen-based alloy backbone at moderate pressure, *Phys. Rev. Lett.* **128**, 047001 (2022).
- [35] B. Ménez, P. Philippot, M. Bonnin-Mosbah, A. Simionovici, and F. Gibert, Analysis of individual fluid inclusions using synchrotron X-ray fluorescence microprobe: Progress toward calibration for trace elements, *Geochim. Cosmochim. Acta* **66**, 561 (2002).
- [36] M. R. Frank, H. P. Scott, E. Aarestad, and V. B. Prakapenka, Potassium chloride-bearing ice VII and ice planet dynamics, *Geochim. Cosmochim. Acta* **174**, 156 (2016).
- [37] G. Shen, Y. Wang, A. Dewaele, C. Wu, D. E. Fratanduono, J. Eggert, S. Klotz, K. F. Dziubek, P. Loubeyre, O. V. Fat’yanov, P. D. Asimow, T. Mashimo, and R. M. M. Wentzcovitch, Toward an international practical pressure scale: A proposal for an IPPS ruby gauge (IPPS-Ruby2020), *High Pressure Res.* **40**, 299 (2020).
- [38] H.-P. Liermann, Z. Konopkova, W. Morgenroth, K. Glazyrin, J. Bednarcik, E. E. McBride, S. Petitgirard, J. T. Delitz, M. Wendt, Y. Bican, A. Ehnes, I. Schwark, A. Rothkirch, M. Fischer, J. Heuer, H. Schulte-Schrepping, T. Kracht, and H. Franz, The extreme conditions beamline P02.2 and the extreme conditions science infrastructure at PETRA III, *J. Synchrotron Radiat.* **22**, 908 (2015).
- [39] C. Prescher and V. B. Prakapenka, DIOPTAS: A program for reduction of two-dimensional X-ray diffraction data and data exploration, *High Pressure Res.* **35**, 223 (2015).
- [40] Y. Fei, A. Ricolleau, M. Frank, K. Mibe, G. Shen, and V. Prakapenka, Toward an internally consistent pressure scale, *Proc. Natl. Acad. Sci. USA* **104**, 9182 (2007).
- [41] G. Kresse and J. Furthmüller, Efficiency of ab-initio total energy calculations for metals and semiconductors using a plane-wave basis set, *Comput. Mater. Sci.* **6**, 15 (1996).
- [42] G. Kresse and D. Joubert, From ultrasoft pseudopotentials to the projector augmented-wave method, *Phys. Rev. B* **59**, 1758 (1999).
- [43] S. Grimme, J. Antony, S. Ehrlich, and H. Krieg, A consistent and accurate *ab initio* parametrization of density functional dispersion correction (DFT-D) for the 94 elements H-Pu, *J. Chem. Phys.* **132**, 154104 (2010).
- [44] J. P. Perdew and Y. Wang, Accurate and simple analytic representation of the electron-gas correlation energy, *Phys. Rev. B* **45**, 13244 (1992).
- [45] J. P. Perdew, K. Burke, and Y. Wang, Generalized gradient approximation for the exchange-correlation hole of a many-electron system, *Phys. Rev. B* **54**, 16533 (1996).
- [46] C. Liu, H. Gao, Y. Wang, R. J. Needs, C. J. Pickard, J. Sun, H.-T. Wang, and D. Xing, Multiple superionic states in helium–water compounds, *Nat. Phys.* **15**, 1065 (2019).
- [47] Q. Zeng, C. Yao, K. Wang, C. Q. Sun, and B. Zou, Room-temperature NaI/H₂O compression icing: Solute–solute interactions, *Phys. Chem. Chem. Phys.* **19**, 26645 (2017).
- [48] J.-M. Léger, J. Haines, and C. Danneels, Phase transition sequence induced by high-pressure in CaCl₂, *J. Phys. Chem. Solids* **59**, 1199 (1998).
- [49] A. Leclaire and M. M. Borel, La forme β du dichlorure de calcium tetrahydrate, *Acta Cryst. B* **34**, 900 (1978).
- [50] See Supplemental Material at <http://link.aps.org/supplemental/10.1103/PhysRevB.109.134108> for the experimental XRD spectra and the Le Bail refinement of the integrated pattern of β -CaCl₂ tetrahydrate (β -CaCl₂ · 4H₂O) at 2.6 GPa and 298 K, the enthalpy difference between each water molecule in the nine configurations and each water molecule in ice VII under different pressures, illustrations of nine different CaCl₂ configurations in ice VII structure after ionic relaxation, and the radial distribution function $g(r)$ of the distance OH below the transition (in phase VII at approximately 20 GPa) in pure ice VII and in Cb VII. The Supplemental Material also contains Ref. [49].
- [51] L. M. Uriarte, J. Dubessy, P. Boulet, V. G. Baonza, I. Bihannic, and P. Robert, Reference Raman spectra of synthesized CaCl₂ · n H₂O solids ($n = 0, 2, 4, 6$), *J. Raman Spectrosc.* **46**, 822 (2015).
- [52] M. Baumgartner and R. J. Bakker, CaCl₂-hydrate nucleation in synthetic fluid inclusions., *Chem. Geol.* **265**, 335 (2009).
- [53] H. Yui, Y. Yoneda, T. Kitamori, and T. Sawada, Spectroscopic analysis of stimulated Raman scattering in the early stage of

- laser-induced breakdown in water, *Phys. Rev. Lett.* **82**, 4110 (1999).
- [54] A. D. Fortes, F. Fernandez-Alonso, M. Tucker, and I. G. Wood, Isothermal equation of state and high-pressure phase transitions of synthetic meridianiite ($\text{MgSO}_4 \cdot 11\text{D}_2\text{O}$) determined by neutron powder diffraction and quasielastic neutron spectroscopy, *Acta Cryst. B* **73**, 33 (2017).
- [55] P. W. Mirwald, Evidence of PVT anomaly boundaries of water at high pressure from compression and $\text{NaCl} \cdot 2\text{H}_2\text{O}$ dehydration experiments, *J. Chem. Phys.* **123**, 124715 (2005).
- [56] G. E. Walrafen, M. Abebe, F. A. Mauer, S. Block, G. J. Piermarini, and R. Munro, Raman and x-ray investigations of ice VII to 36.0 GPa, *J. Chem. Phys.* **77**, 2166 (1982).
- [57] P. Ph, J. C. Chervin, and M. Gauthier, Raman spectroscopy investigation of ice VII and deuterated ice VII to 40 GPa. Disorder in ice VII, *Europhys. Lett.* **13**, 81 (1990).
- [58] X. Li, W. Shi, X. Liu, and Z. Mao, High-pressure phase stability and elasticity of ammonia hydrate, *Am. Mineral.* **104**, 1307 (2019).
- [59] M. R. Frank, Y. Fei, and J. Hu, Constraining the equation of state of fluid H_2O to 80 GPa using the melting curve, bulk modulus, and thermal expansivity of Ice VII, *Geochim. Cosmochim. Acta* **68**, 2781 (2004).
- [60] P. Pruzan, J. C. Chervin, E. Wolanin, B. Canny, M. Gauthier, and M. Hanfland, Phase diagram of ice in the VII–VIII–X domain. Vibrational and structural data for strongly compressed ice VIII, *J. Raman Spectrosc.* **34**, 591 (2003).
- [61] K. Momma and F. Izumi, VESTA 3 for three-dimensional visualization of crystal, volumetric and morphology data, *J. Appl. Crystallogr.* **44**, 1272 (2011).
- [62] J. L. Lyons and C. G. Van de Walle, Computationally predicted energies and properties of defects in GaN, *npj Comput. Mater.* **3**, 12 (2017).
- [63] Y. Bronstein, P. Depondt, F. Finocchi, and A. M. Saitta, Quantum-driven phase transition in ice described via an efficient Langevin approach, *Phys. Rev. B* **89**, 214101 (2014).
- [64] K. R. Hirsch and W. B. Holzapfel, Effect of high pressure on the Raman spectra of ice VIII and evidence for ice X, *J. Chem. Phys.* **84**, 2771 (1986).
- [65] W. Shi, N. Sun, X. Li, Z. Mao, J. Liu, and V. B. Prakapenka, Single-crystal elasticity of high-pressure ice up to 98 GPa by Brillouin scattering, *Geophys. Res. Lett.* **48**, e2021GL092514 (2021).
- [66] M. R. Frank, H. P. Scott, S. J. Maglio, V. B. Prakapenka, and G. Shen, Temperature induced immiscibility in the NaCl – H_2O system at high pressure, *Phys. Earth Planet Inter.* **170**, 107 (2008).
- [67] A. F. Goncharov, N. Goldman, L. E. Fried, J. C. Crowhurst, I. F. W. Kuo, C. J. Mundy, and J. M. Zaug, Dynamic ionization of water under extreme conditions, *Phys. Rev. Lett.* **94**, 125508 (2005).
- [68] A. F. Goncharov, V. V. Struzhkin, H.-k. Mao, and R. J. Hemley, Raman spectroscopy of dense H_2O and the transition to symmetric hydrogen bonds, *Phys. Rev. Lett.* **83**, 1998 (1999).
- [69] T. M. Orlando, T. B. McCord, and G. A. Gieves, The chemical nature of Europa surface material and the relation to a subsurface ocean, *Icarus* **177**, 528 (2005).
- [70] O. Ozgurel, O. Mousis, F. Pauzat, Y. Ellinger, A. Markovits, S. Vance, and F. Leblanc, Sodium, potassium, and calcium in Europa: An atomic journey through water ice, *Astrophys. J. Lett.* **865**, L16 (2018).
- [71] X. Wei, Dataset for: Impact of CaCl_2 -induced chemical pressure on the phase transition of H_2O at high pressure (Zenodo, 2023), doi:10.5281/zenodo.10076902.